Nov 22, 2021

Thanks again for your helpful and valuable comments on our manuscript entitled “The Spatiotemporal Regime of Glacier Runoff in Oases Indicates the Potential Climatic Risk in Dryland Areas of China” (ID: HESS-2021-377). After studying your comments carefully, we have made some corrections which we hope to meet with approval.

(1) First of all, we rewrite the Methods and annotate parameters correctly. As for some details we have discussed too much, such as the reasons for choosing Shean Estimation and APHRODITE, we use charts and figures to illustrate them in supplementary materials. We also add the methods to calculate the glacier area change. The revised Methods with supplementary materials read as:

“2.3 Methods

2.3.1 Ablation on glaciers

Glacier ablation at different time steps is obtained from the degree-day factor (DDF) model, namely, the product of the DDF and positive-degree days (PDD) (Braithwaite & Olesen, 1993) summing positive daily average temperatures at different time steps as shown in Eq. (1)-(3):

$$A_{b,y} = DDF \times PDD_y, \quad (1)$$

$$PDD = \sum_{t=1}^{n} H_t \cdot T_{a,t}, \quad (2)$$

$$H_t = \begin{cases} 1.0, T_{a,t} \geq 0 \\ 0.0, T_{a,t} < 0 \end{cases}, \quad (3)$$

where H_t is a logistic variable, t refers to the time scale, $T_{a,t}$ is the temperature corrected by DEM (decreased 0.65 degrees per 100 m altitude rise).

The DDF is an important parameter reflecting the amount of ice and snow melt generated by the unit positive accumulated temperature (Kaser et al., 2010; Kraaijenbrink et al., 2017). Previous studies have generally used 2 mm $°C^{-1}$ d^{-1} as the DDF of the ice-coved glacier and 7 mm $°C^{-1}$ d^{-1} as the DDF of the debris-covered glacier (Azam et al., 2012; Immerzeel et al., 2015). The spatial variation in the DDF has a great influence on the accuracy of simulating the snowmelt process. This paper used the spatial distribution of $DDFs$ for glaciers with a resolution of 0.5° based on a formula built by investigations and observations of 40 different glaciers in the HMA. Map of isolines for the DDFs shows

the factors increase gradually from northwest to southeast in western China which is consistent with the varied climatic environment from cold-dry to warm-wet (Zhang et al., 2006). Monthly positive-degree days (PDD_m) were chosen instead of absolute daily PDD while the calculation method was still summing positive daily average temperatures, on the 100 m grid scale consistent with the spatial resolution of DEM.

2.3.2 Accumulation on glaciers

In this paper, the maximum precipitation height (H_{map}) was introduced as a parameter for calculating accumulation. The H_{map} of each glacier region around the DAC was obtained from previous studies (Chen et al., 2018; Hewitt, 2007; Immerzeel et al., 2012; Wang et al., 2019; Zhang, Tuerxunbai, et al., 2019). For each glacier, the precipitation is lapsed from its maximum height (H_{max}) to its H_{map} negatively with the same precipitation gradient (PG). On basis of each glacier range in the form of shapefile from RGI v6.0, high-altitude reconciled precipitation at different altitudes was calculated as Eq. (4):

$$P_{cor,d} = \begin{cases} P_{rmd,d} \cdot [1 + (H_{max} - H) \cdot PG \cdot 0.01], H > H_{map} \\ P_{rmd,d} \cdot \left[1 + \left(H_{map} - H\right) \cdot PG \cdot 0.01\right], H \le H_{map} \end{cases} \quad (4)$$

where $P_{rmd,d}$(m) is original precipitation from APHRODITE, H_{max}(m) is the maximum height of each glacier from RGI, H(m) is the altitude from DEM at a grid scale, PG(% m^{-1}) is the vertical precipitation gradient for each glacier, and H_{map}(m) is the maximum precipitation height of each glacier region based on previous studies.

Original calculation of atmospheric accumulation on glaciers depends on temperature, by which precipitation is separated into solid (snow, A_c(m)) and liquid (rain). The temperature at which all precipitation becomes liquid was assumed to be 4°C, T_1(°C). The calculation for accumulation on glacier was following Eq. (5) (Fujita & Nuimura, 2011; Sakai et al., 2015):

$$A_{c,d} = \begin{cases} P_{cor,d}, T_a \le 0 \\ \left(1 - \frac{T_a}{T_1}\right) P_{cor,d}, 0 < T_a \le T_1, \\ 0, T_a > T_1 \end{cases} \quad (5)$$

where T_a(°C) is the actual temperature corrected by DEM, $P_{cor,d}$(m) is the daily corrected precipitation, T_1(°C) is set to 4, and $A_{c,d}$(m) is accumulation on glacier at a daily step.

2.3.3 Mass balance

We used regional available glacier mass balance dataset to correct high-altitude precipitation. The mass balance, B_y(m), is the sum of accumulation, $A_{c,y}$(m), and ablation, $A_{b,y}$(m), at a yearly time step of each glacier following Eq. (6):

$$B_y = A_{b,y} + A_{c,y}, \quad (6)$$

Existing regional glacier mass balance datasets included those produced by Brun et al. (2017), based on ASTER DEMs from 2000 to 2016 at a spatial resolution of 30 m (hereafter, Brun estimation), by Shean et al. (2020), extending Brun Estimation to 2018 for each glacier in RGI (hereafter, Shean estimation), and based on NASA's Ice, Cloud and Land Elevation Satellite (ICESat-1) data for the period 2003-2008 (hereafter, IceSat data) (Immerzeel et al., 2015; Kääb et al., 2012; Srivastava et al., 2013). A comparison of the former three datasets was shown in Extended Table1 and Extended Figure 1. This paper selected the Shean estimation to simulate mass balance using the mass balance and uncertainty of each glacier, which was based on multisource RGI v6.0 glacier inventory (while the Brun estimation used the single-source GAMDAM inventory) and implemented robust approaches to estimate elevation change trends for each glacier.

2.3.4 Reconciling High-altitude Precipitation

Annual yearly glacier ablation from 2000 to 2018 was calculated by Eq. (1)-(4), meanwhile, the annual yearly glacier mass balance from 2000 to 2018 was provided by Shean estimation. According to Eq. (6), the annual yearly accumulation ($A_{c,y}$) of each glacier for the same period could be obtained. By substituting $A_{c,y}$ into Eq. (4) and Eq. (5), the PG of each glacier in RGI can be collected with the support of DEM and APHRODITE. The spatial resolution of APHRODITE was quite different from that of DEM. To reduce the impact of grid mutation from precipitation data, the nearest neighbor algorithm (López-Granados et al., 2005) was used to aggregate, and the map of PG was obtained at a regional scale.

2.3.5 Glacier Runoff

Substituting the map of PG, original precipitation and temperature from APHRODITE, and DEM into Eq. (1)-(6), the time-series of mass balance for each glacier could be obtained.

To be precise, glacier runoff including meltwater runoff and delayed runoff in this study is runoff generated within the glacier range, where glacier areas change over time. Delayed runoff was caused by remaining precipitation which stored

as snow in cold seasons and discharged in warm seasons after offsetting ablation (Kaser et al., 2010; Pritchard, 2019; Shean et al., 2020), and also included part of precipitation in warm seasons. Meltwater runoff, which was also called excessive meltwater runoff or the imbalanced part of glacier runoff, was caused by mass loss of glaciers when atmospheric accumulation cannot offset ablation on glaciers.

Glacier runoff, G_m(m), during warm seasons was calculated according to the proportion of monthly PDD, PDD_m, to yearly PDD, PDD_y, and the absolute value of yearly mass balance at each grid cell of 100 m as the following Eq. (7):

$$G_m = \left|B_y\right| \times PDD_m / PDD_y, \quad (7)$$

Monthly delayed runoff, D_m(m), was the product of B_y greater than zero and the proportion of PDD_m to PDD_y; Accordingly, meltwater runoff, M_m, was the product of B_y less than zero and the proportion of PDD_m to PDD_y as shown in Eq. (8) and Eq. (9):

$$D_m = B_y \times PDD_m / PDD_y \, , B_y \geq 0, \quad (8)$$

$$M_m = B_y \times PDD_m / PDD_y \, , B_y < 0, \quad (9)$$

In this paper, we present a method to obtain a time series of runoff including delayed runoff and meltwater runoff generating in glacier regions after reconciling high-altitude precipitation by existing glacier mass balance dataset, Shean estimation, which makes up for the problem of datasets that were incomprehensive (only mass balance) or semi-quantitative (only glacier runoff proportion) in glacier areas at a regional scale. This dataset can be used in hydrological models to better simulate the whole hydrological process.

2.3.6 Glacier Area Change

Glacier outlines were extracted from Landsat TM scenes in the two periods (Region1985-1995 and Region1995-2005) in each basin at the end of ablation seasons (September to November), respectively, in Google Earth Engine™ (hereafter, GEE) based on band ratio segmentation method (Guo et al., 2015; Paul et al., 2009; Racoviteau et al., 2009). We used the value of 2.0 to differentiate glacier and non-glacier as the threshold for TM3/TM5 within a three-pixel buffer of the glacier outline of RGI. As the Scan-Line Corrector (SLC) within the ETM+ instrument failed in May, all images after that time

have offset scans, appearing as strips of zero radiance that widen toward the edge of the image, which severely affected the use of Landsat ETM+ remote sensing images. Glacier outlines of RGI were set for the glacier range in the period of 2005-2015 (Region2005-2015) considering the Landsat imageries used in RGI from 2005-2015 in general (Dates of Landsat imageries used in RGI in different river basins was shown in Extended Table 2).

2.3.7 Total uncertainty Analysis

According to the individual glacier uncertainty (including random error and systematic error) calculated in the Shean estimation, the uncertainty range of glacier mass balance changes could be obtained. Using the same routine which was described in 2.3.4 to calculate distributions of PG corresponding to the maximum and minimum mass balance values from Shean estimation, and time-series of maximum and minimum glacier runoff generated by the map of corresponding PG were obtained by substituting original precipitation and temperature from APHRODITE and DEM into Eq. (1)-(9). Calculations of delayed runoff and meltwater runoff and their uncertainties were shown in Fig. 2 where shaded blocks were results with uncertainties.

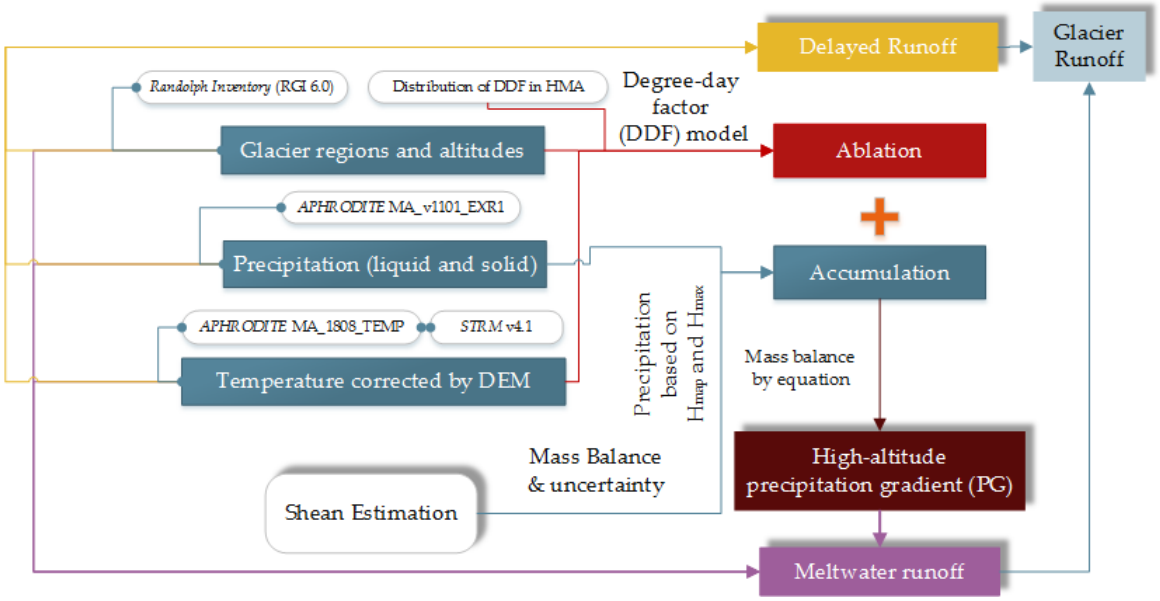

Fig. 2. Conceptual framework of glacier runoff calculating. Blocks represent modules of the glacier runoff calculation in each category. Shading indicated results with uncertainties and different lines and blocks indicated the corresponding modules.

2.3.8 Trend Analysis

The Mann-Kendall test (MK test) was recommended as an effective method to distinguish whether a natural process is in a natural fluctuation or has a definite trend of change especially for hydro-meteorological data with non-normal distribution (Mann, 1945; Kendall, 1975). Given a time series $x(t)$ of length n with statistical hypothesis that the unadjusted data series was an independent random variable with the same distribution composed of n elements. m_i represented the cumulative number of $x(i)$ was greater than $x(j), 1 \le j \le i$, and the statistic d_k was defined as following Eq. (10):

$$d_k = \sum_{i=1}^{k} m_i, 2 \le k \le n, \tag{10}$$

The mean $E(d_k)$ and variance $var(d_k)$ was calculated by the following Eq. (11) and Eq. (12):

$$E(d_k) = k(k-1)/4, \tag{11}$$

$$\mathrm{var}(d_k) = k(k-1)(2k+5)/72, \tag{12}$$

After standardizing d_k, UF_k and UB_k can be calculated as following Eq. (13) and Eq. (14):

$$UF_k = \frac{d_k - E(d_k)}{\sqrt{var(d_k)}}, \tag{13}$$

$$\begin{cases} UB_k = -UF_k \\ k = n+1-k, k = 1,2,3,\cdots,n' \end{cases} \tag{14}$$

UF_k formed a UF curve and UB_k formed a UB curve, while the intersection point of the former two curves in the confidence interval was determined as the turning point. While $UF > 0$, it indicated an increasing trend of the sequence, on the contrary, it indicated a declining trend while $UF < 0$.

Extended Table 1

Comparison about mass balance datasets in different glacier regions

RGI regions	MB from IceSat [2003-2009]	MB from Brun (Aster) [2000-2016]	MB from Shean (Aster-SPOT) [2000-2018]
13-01 Hissar Alay	-0.12±0.24	-0.04±0.07	-0.03±0.20
13-02 Pamir		-0.06±0.07	-0.05±0.09
13-03 W Tien Shan	-0.52±0.24	-0.20±0.08	-0.22±0.33
13-04 E Tien Shan		-0.40±0.20	-0.42±0.25
13-05 W Kun Lun	0.16±0.18	0.16±0.08	0.10±0.17
13-06 E Kun Lun	-0.01±0.15	-0.01±0.07	-0.02±0.15
13-07 Qilian Shan	-0.29±0.33	-0.29±0.08	-0.29±0.25
13-08 Inner Tibet	-0.01±0.15	-0.19±0.08	-0.24±0.21
13-09 S an E Tibet	-0.27±0.16	-0.55±0.23	-0.48±0.32
14-01 Hindu Kush	-0.10±0.18	-0.13±0.07	-0.13±0.17
14-02 Karakoram		-0.03±0.07	-0.05±0.13
14-03 W Himalaya	-0.48±0.17	-0.38±0.09	-0.36±0.11
15-01 C Himalaya	-0.40±0.23	-0.28±0.08	-0.28±0.15
15-02 E Himalaya	-0.80±0.22	-0.38±0.20	-0.35±0.20
15-03 Hengduan Shan	-0.36±0.43	-0.56±0.23	-0.50±0.15

Extended Figure 1

Mass balance in different glacier regions

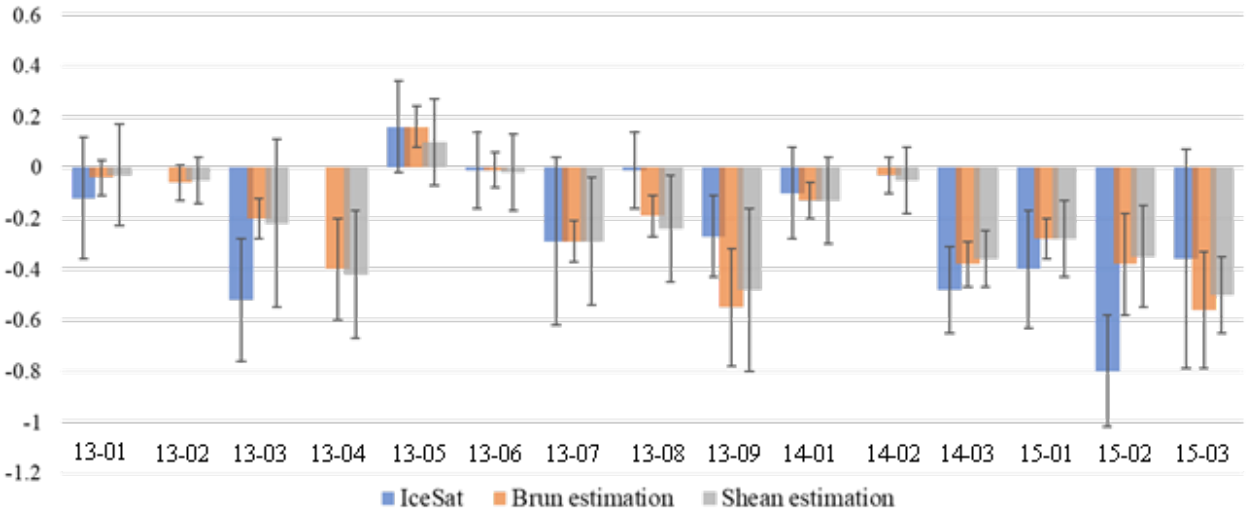

While the ICESat data did not reflect small glaciers, the data were used to calculate the elevation changes of glaciers larger than 5 km^2 in area and then to interpolate the elevation variations across the entire region, and the satellite no longer provided data in 2009. As the algorithms of the Brun estimation and Shean estimation were analogous, this paper focused on comparing the Shean estimation and Brun estimation to handle a more appropriate dataset. There was little difference in overall mass balance between the two datasets (-0.87 of Brun estimation and -0.98 of Shean estimation in our study area), but a great difference in uncertainties in some regions such as in Western Tien Shan (0.08 of Brun estimation and 0.33 of Shean estimation) and Qilian Shan (0.08 of Brun estimation and 0.25 of Shean estimation). We chose Shean estimation since it provided mass balance of each glacier in RGI while Brun provided distribution images with a resolution of 30 m.

Extended Table 2

Dates of Landsat imageries used in RGI

ID	Basin	Image Date
1	Middle Rivers Basin	20070911, 20070913, 20090723, 20090725, 20090808, 20090826, 20100813
2	Yarkand River Basin	19980813, 19980820, 20000902, 20000904, 20000911, 20010721, 20020802, 20070729, 20080731, 20090726, 20090811, 20090921, 20090930, 20100823, 20100917
3	Western Qaidam Basin	20060723, 20060909, 20060914, 20070504, 20070731, 20070811, 20070825, 20070903, 20070919, 20070921, 20090830, 20090901, 20100428, 20100806, 20100831, 20100902
4	Eastern Qaidam Basin	20060723, 20070921, 20080830
5	Datong River Above Xiangtang	20070813, 20090617
6	Eastern Rivers Basin	20060811, 20100813
7	Ebinur Lake Drainage System	19990918, 20070824, 20070911, 20070916, 20070918, 20070920, 20090723, 20090808, 20090813
8	Hami Basin	20070825, 20100824
9	Heihe River Basin	20050909, 20060909, 20060918, 20060920, 20070813, 20070822, 20100727
10	Hotan River Basin	20020802, 20080903, 20090603, 20090813, 20090907, 20090921, 20090930, 20100823, 20100917, 20101129, 20101208, 20110805
11	Ili River Basin	20020818, 20070824, 20070911, 20070916, 20070918, 20070925, 20090723, 20090808, 20090813, 20091002
12	Kai-kong River Basin	20070515, 20070911, 20070913, 20090723, 20090801, 20090808, 20090817
13	Kashgar River Basin	20000824, 20000902, 20000911, 20010726, 20010820, 20010928, 20070923, 20090701, 20090726, 20090910, 20090919
14	Kriya Rivers Basin	20070819, 20090907, 20101208, 20110805
15	Pai Basin	20070825, 20100824
16	Qarqan Rivers Basin	20070508, 20070517, 20070625, 20070819, 20100806, 20100813, 20100831, 20100907
17	Qinghaihu Lake Drainage System	20060918, 20070813, 20080830
18	Shiyang River Basin	20090617
19	Shule River Basin	20060909, 20060918, 20070813, 20070825, 20070903, 20090901
20	Turpan Basin	20060811, 20070913, 20090801, 20090817, 20090819, 20090826, 20100813
21	Weigan River Basin	20020818, 20070824, 20070911, 20070918
22	Aksu River Basin	19990808, 20020724, 20020818, 20020825, 20021003, 20070824, 20070907, 20070916, 20070923

”

(2) We add the analysis of changes in glacier areas. Glacier outlines were extracted from Landsat TM scenes in the two periods (Region1985-1995 and Region1995-2005) in each basin at the end of ablation seasons (September to November), respectively, in Google Earth EngineTM (hereafter, GEE) based on band ratio segmentation method (Guo et al., 2015; Paul et al., 2009; Racoviteau et al., 2009). The distribution of different sizes in different basins is shown in the following figure:

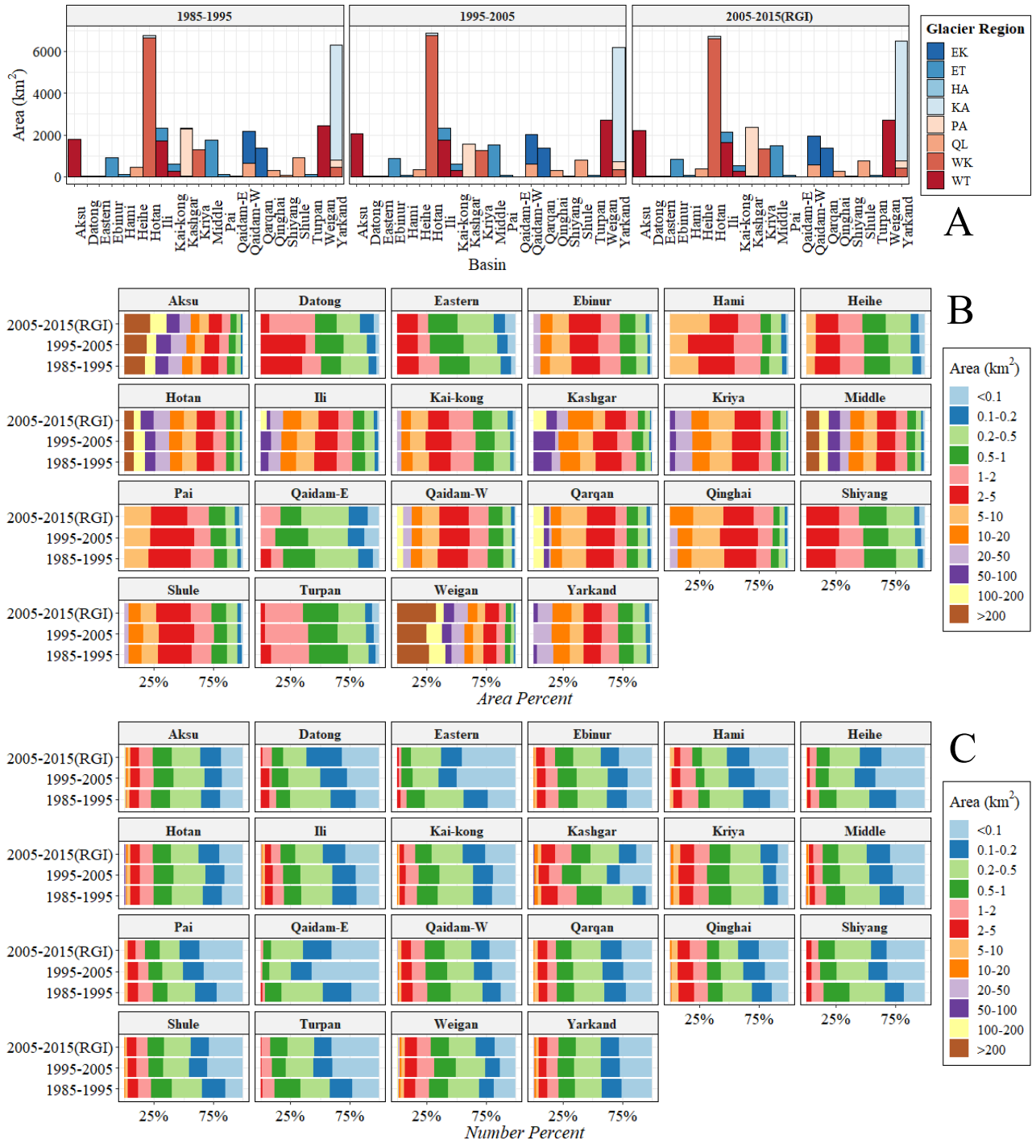

Note. Total glacier areas in different basins from different glacier regions (A) and respective proportions of numbers (B) and area (C) within different basins in three periods (1985-1995, 1995-2005, 2005-2015 (RGI)).

We also add an analysis of changes in glacier area in Results. It reads as:

"**Glacier Area Change**

In the RGI, 53749 glaciers were compiled with a total area of 32008 km^2 in our study area. Hotan River Basin has the largest glacier area (6719.50 km^2), and Yarkand River Basin has the largest number of glaciers (4487). Figure A shows the glacier area in each watershed that originated from different glacier regions in three periods (1985-1995, 1995-2005, 2005-2015). The general characteristics of glacier size distribution are that large numbers of small glaciers account for a small proportion of the total area, while there are less numbers of large glaciers that account for a large proportion of the total area (Bliss et al., 2013; Guo et al., Hagg et al., 2013; 2015; Le Bris et al., 2011; Paul et al., 2009). The feature is also clear in our study area especially in Aksu River Basin, Hotan River Basin, and Weigan River Basin as shown in Figures B and C. It can be seen that glaciers in the DAC are mainly less than 1 km^2, accounting for 70% or more of the total glacier area in the corresponding basin. Except for Datong River Above Xiangtang, Eastern Rivers Basin, Eastern Qaidam Basin, Shiyang River Basin, Turpan Basin, and Ebinur Lake Drainage System, the glaciers larger than 2 km^2 accounts for 50% or more of each basin.

During the three periods, the number proportion of glaciers smaller than 1 km^2 increases gradually, except in the Aksu River Basin, Hotan River Basin, Weigan River Basin, and Kriya Rivers Basin which are controlled by glaciers larger than 5 km^2, and Yarkand River Basin and Kashgar River Basin which are hindered by the date of remote sensing images. The area proportion of glaciers in Yarkand River Basin controlled by Karakoram, and Qarqan Rivers Basin and Western Qaidam Basin which are controlled by Eastern Kunlun remained almost unchanged, as Karakoram remains relatively stable, which is called the "Karakoram anomaly" (Hewitt, 2005) and Eastern Kunlun has a positive mass balance (Brun et al., 2017; Shean et al., 2020). The area proportion of glaciers larger than 5 km^2 in Aksu River Basin, Hotan River Basin, Ili River Basin, Kashgar River Basin, Middle Rivers Basin, and Weigan River Basin which are controlled by large glaciers increases with the periods. The area proportion of glaciers smaller than 1 km^2 in Heihe River Basin, Eastern Qaidam Basin, Shiyang River Basin, Eastern Rivers Basin, and Turpan Basin increases period by period. The higher area proportions of > 1 km^2 glaciers in these basins also illustrate the dominance of small glaciers."

References:

Azam, M. F., Wagnon, P., Ramanathan, A., Vinicent, C., Sharma, P., Arnaud, Y., Linda, A., Pottakkal, J. G., Chevallier, P., Singh, V. B., and Berthier, E.: From balance to imbalance: a shift in the dynamic behaviour of Chhota Shigri glacier, western Himalaya, India, J. Glaciol., 58, 315-324, doi: 10.3189/2012JoG11J123, 2012.

Bliss, A., Hock, R., and Cogley, J. G.: A new inventory of mountain glaciers and ice caps for the Antarctic periphery, Ann. Glaciol., 54(63), 191-199, doi: 10.3189/2013AoG63A377, 2013.

Braithwaite, R. J. and Olesen, O. B.: Seasonal variation of ice ablation at the margin of the Greenland ice sheet and its sensitivity to climate change, Qamanârssûp sermia, West Greenland, J. Glaciol., 39, 267-274, doi: 10.3189/S0022143000015938, 1993.

Brun, F., Berthier, E., Wagnon, P., Kääb, A., and Treichler, D.: A spatially resolved estimate of High Mountain Asia glacier mass balances from 2000 to 2016, Nat. Geosci., doi: 10, 668-673, 10.1038/ngeo2999, 2017.

Chen, R., Han, C., Liu, J., Yang, Y., Liu, Z., Wang, L., and Kang, E.: Maximum precipitation altitude on the northern f lank of the Qilian Mountains, northwest China, Hydrol. Res., 49, 1696-1710, doi: 10.2166/nh.2018.121, 2018.

Fujita, K. and Nuimura, T.: Spatially heterogeneous wastage of Himalayan glaciers, P. Natl. Acad. Sci. USA, doi: 108, 14011, 10.1073/pnas.1106242108, 2011.

Guo, W. Q., Liu, S. Y., Xu, J. L., Wu, L. Z., Shangguan, D. H., Yao, X. J., Wei, J. F., Bao, W. J., Yu, P. C., Liu, Q. and Jiang, Z. L.: The second Chinese glacier inventory: data, methods and results, J. Glacio., 61, 357-372, doi: 10.3189/2015JoG14J209, 2015.

Hagg, W., Mayer, C., Lambrecht, A., Kriegel, D., and Azizov, E.: Glacier changes in the Big Naryn basin, Central Tian Shan, Global Planet. Change, 110A, 40-50, doi: 10.1016/j.gloplacha.2012.07.010, 2013.

Hewitt, K.: The Karakoram Anomaly? Glacier Expansion and the 'Elevation Effect,' Karakoram Himalaya, Mountain Research and Development, 25(4), 332-340, doi: 10.1659/0276-4741(2005)025[0332:TKAGEA]2.0.CO;2, 2005.

Hewitt, K.: Tributary glacier surges: an exceptional concentration at Panmah Glacier, Karakoram Himalaya, J. Glaciol., 53, 181-188, doi: 10.3189/172756507782202829, 2007.

Immerzeel, W. W., van Beek, L. P. H., Konz, M., Shrestha, A. B., and Bierkens, M. F. P.: Hydrological response to climate change in a glacierized catchment in the Himalayas, Clim. Change, 110, 721-736, doi: 10.1007/s10584-011-0143-4, 2012.

Immerzeel, W. W., Wanders, N., Lutz, A. F., Shea, J. M., and Bierkens, M. F. P.: Reconciling high-altitude

precipitation in the upper Indus basin with glacier mass balances and runoff, Hydrol. Earth Syst. Sci., 19, 4673-4687, doi: 10.5194/hess-19-4673-2015, 2015.

Kääb, A., Berthier, E., Nuth, C., Gardelle, J., and Arnaud, Y.: Contrasting patterns of early twenty-first-century glacier mass change in the Himalayas, Nature, 488, 495-498, doi: 10.1038/nature11324, 2012.

Kaser, G., Großhauser, M., and Marzeion, B.: Contribution potential of glaciers to water availability in different climate regimes, P. Natl. Acad. Sci. USA, 107, 20223, doi: 10.1073/pnas.1008162107, 2010.

Kendall, M. G. :Rank correlation methods, Charles Griffin, London, 1975.

Kraaijenbrink, P. D. A., Bierkens, M. F. P., Lutz, A. F., and Immerzeel, W. W.: Impact of a global temperature rise of 1.5 degrees Celsius on Asia's glaciers, Nature, 549, 257-260, doi: 10.1038/nature23878, 2017.

Le Bris, R., Paul, F., Frey, H., and Bolch, T.: A new satellite-derived glacier inventory for western Alaska, Ann. Glaciol., 52(59), 135-143, doi: 10.3189/172756411799096303, 2011.

López-Granados, F., Jurado-Expósito, M., Peña-Barragán, J. M., and García-Torres, L.: Using geostatistical and remote sensing approaches for mapping soil properties, Eur. J. Agron., 23, 279-289, doi: 10.1016/j.eja.2004.12.003, 2005.

Mann, H. B.: Nonparametric Tests Against Trend, Econometrica, 13, 245-259, doi: 10.2307/1907187, 1945.

Paul, F., Barry, R. G., Cogley, J. G., Frey, H., Haeberli, W., Ohmura, A., Ommanney, C. S. L., Raup, B., Rivera, A., and Zemp, M.: Recommendations for the compilation of glacier inventory data from digital sources, Ann. Glaciol., 50(53), 119-126, doi: 10.3189/172756410790595778, 2009.

Pritchard, H. D.: Asia's shrinking glaciers protect large populations from drought stress, Nature, 569, 649-654, doi: 10.1038/s41586-019-1240-1, 2019.

Racoviteanu, A. E., Paul, F., Raup, B., Khalsa, S. J. S., and Armstrong, R.: Challenges and recommendations in mapping of glacier parameters from space: results of the 2008 Global Land Ice Mesurements from Space (GLIMS) workshop, Boulder, Colorado, USA, Ann. Glaciol., 50(53), 53-69, doi: 10.3189/172756410790595804, 2009.

Sakai, A., Nuimura, T., Fujita, K., Takenaka, S., Nagai, H., and Lamsal, D.: Climate regime of Asian glaciers revealed by GAMDAM glacier inventory, Cryosphere, 9, 865-880, doi: 10.5194/tc-9-865-2015, 2015.

Shean, D. E., Bhushan, S., Montesano, P., Rounce, D. R., Arendt, A., and Osmanoglu, B.: A Systematic, Regional Assessment of High Mountain Asia Glacier Mass Balance, Front. Earth Sci., 7, 363, doi: 10.3389/feart.2019.00363, 2020.

Srivastava, P., Bhambri, R., Kawishwar, P., and Dobhal, D. P.: Water level changes of high altitude lakes in Himalaya–Karakoram from ICESat altimetry, Journal of Earth System Science, 122, 1533-1543, doi:

10.1007/s12040-013-0364-1, 2013.

Wang, R., Liu, S., Shangguan, D., Radić, V., and Zhang, Y.: Spatial Heterogeneity in Glacier Mass-Balance Sensitivity across High Mountain Asia, Water, 11, doi: 10.3390/w11040776, 2019.

Zhang, Y., Liu, S., and Ding, Y.: Observed degree-day factors and their spatial variation on glaciers in western China, Ann. Glaciol., 43, 301-306, doi: 10.3189/172756406781811952, 2006.

Zhang, Y., Tuerxunbai, G., Su, L., and Qianqian, L.: Spatial and temporal characteristics of climate change at different altitudes in Xinjiang in the past 60 years, Arid Land Geography (in Chinese), 42, 822-829: doi: 10.12118/j.issn.1000-6060.2019.04.13, 2019.